



Article

Nickel-Containing Perovskites, $\text{PrNi}_{0.4}\text{Fe}_{0.6}\text{O}_{3-\delta}$ and $\text{PrNi}_{0.4}\text{Co}_{0.6}\text{O}_{3-\delta}$, as Potential Electrodes for Protonic Ceramic Electrochemical Cells

Artem P. Tarutin ^{1,2,*} , Anna V. Kasyanova ^{1,2}, Gennady K. Vdovin ¹, Julia G. Lyagaeva ^{1,2} and Dmitry A. Medvedev ^{3,*} 

¹ Laboratory of Electrochemical Devices Based on Solid Oxide Proton Electrolytes, Institute of High Temperature Electrochemistry, 620990 Ekaterinburg, Russia

² Chemical Engineering Institute, Ural Federal University, 620002 Ekaterinburg, Russia

³ Hydrogen Energy Laboratory, Ural Federal University, 620002 Ekaterinburg, Russia

* Correspondence: vanomass333@gmail.com (A.P.T.); dmitrymedv@mail.ru (D.A.M.)

Abstract: Protonic ceramic fuel cells (PCFCs) offer a convenient means of converting chemical energy into electricity with high performance and efficiency at low- and intermediate-temperature ranges. However, in order to ensure good life-time stability of PCFCs, it is necessary to ensure rational chemical design in functional materials. Within the present work, we propose new Ni-based perovskite phases of $\text{PrNi}_{0.4}\text{M}_{0.6}\text{O}_{3-\delta}$ (where M = Co, Fe) for potential utilization in protonic ceramic electrochemical cells. Along with their successful synthesis, functional properties of the $\text{PrNi}_{0.4}\text{M}_{0.6}\text{O}_{3-\delta}$ materials, such as chemical compatibility with a number of oxygen-ionic and proton-conducting electrolytes, thermal expansion behavior, electrical conductivity, and electrochemical behavior, were comprehensively studied. According to the obtained data, the Co-containing nickelate exhibits excellent conductivity and polarization behavior; on the other hand, it demonstrates a high reactivity with all studied electrolytes along with elevated thermal expansion coefficients. Conversely, while the iron-based nickelate had superior chemical and thermal compatibility, its transport characteristics were 2–5 times worse. Although, $\text{PrNi}_{0.4}\text{Co}_{0.6}\text{O}_{3-\delta}$ and $\text{PrNi}_{0.4}\text{Fe}_{0.6}\text{O}_{3-\delta}$ represent some disadvantages, this work provides a promising pathway for further improvement of Ni-based perovskite electrodes.

Keywords: PCFCs; PrNiO_3 ; EIS; compatibility; electrodes



Citation: Tarutin, A.P.; Kasyanova, A.V.; Vdovin, G.K.; Lyagaeva, J.G.; Medvedev, D.A. Nickel-Containing Perovskites, $\text{PrNi}_{0.4}\text{Fe}_{0.6}\text{O}_{3-\delta}$ and $\text{PrNi}_{0.4}\text{Co}_{0.6}\text{O}_{3-\delta}$, as Potential Electrodes for Protonic Ceramic Electrochemical Cells. *Materials* **2022**, *15*, 2166. <https://doi.org/10.3390/ma15062166>

Academic Editor: Ana Belen Munoz Garcia

Received: 16 February 2022

Accepted: 12 March 2022

Published: 15 March 2022

Publisher's Note: MDPI stays neutral with regard to jurisdictional claims in published maps and institutional affiliations.



Copyright: © 2022 by the authors. Licensee MDPI, Basel, Switzerland. This article is an open access article distributed under the terms and conditions of the Creative Commons Attribution (CC BY) license (<https://creativecommons.org/licenses/by/4.0/>).

1. Introduction

Research into the use of hydrogen as an energy vector continues to increase worldwide as part of rational efforts aimed at balancing the negative impacts of industrial lifestyles with the constant demand for novel energy sources [1–3]. In response to increasing risks of global warming and climate change, a number of large-scale hydrogen energy programs have been established over the past few years [4–6]. Projects implemented within such programs involve the manipulation of hydrogen and hydrogen-related compounds, including their safe production, storage, transportation, and utilization [7,8]. From this viewpoint, high-temperature electrochemical devices such as solid oxide fuel cells (SOFCs) and electrolysis cells (SOECs), belonging to a broad canvas of hydrogen-related energy approaches, represent one of the most efficient means of energy-conversion for various purposes [9–11].

Having been well-studied in terms of fundamental science, conventional SOFCs based on zirconia-based electrolytes are now produced on an industrial scale [12–14]. Nevertheless, their relatively high operating temperatures (above 800 °C) result in a certain life-time degradation associated both with interchemical diffusion effects and various microstructural changes [15–17]. In this regard, many research efforts have been aimed at

decreasing SOFC operating temperatures to intermediate- or low-temperature ranges in order to eliminate such degradation issues [18–20]. Here, one of the possible approaches consists in the design of SOFCs based on proton-conducting electrolytes (so-called protonic ceramic fuel cells or PCFCs), which offer desirable performance at reduced operational temperatures due to the high ionic conductivity as a result of proton transportation [21–24]. Despite the attractiveness of PCFCs, the selection of suitable electrode materials continues to be problematic due to the need to combine superior electrochemical performance with satisfactory compatibility [25–29].

In the present work, we characterize $\text{PrNi}_{0.4}\text{M}_{0.6}\text{O}_{3-\delta}$ (where $\text{M} = \text{Fe}, \text{Co}$) compounds as possible electrode materials for PCFCs. The justification for selecting these compositions is based on the parent lanthanum-based perovskite phases, i.e., $\text{LaNi}_{1-x}\text{Fe}_x\text{O}_{3-\delta}$ (LNF), which demonstrate a good combination between thermal expansion and electrical conductivity [30–34]. In detail, LNF exhibit extremely low thermal expansion coefficients (around $(11.5\text{--}12.5)\cdot 10^{-6} \text{ K}^{-1}$ [30]) compared to complex oxides based on simple ($\text{Ba}_{0.5}\text{Sr}_{0.5}\text{CoO}_{3-\delta}$, $\text{Ba}_{0.5}\text{Sr}_{0.5}\text{Co}_{0.8}\text{Fe}_{0.2}\text{O}_{3-\delta}$) or double ($\text{GdBaCo}_2\text{O}_{5+\delta}$, $\text{NdBa}_{0.5}\text{Sr}_{0.5}\text{Co}_{1.5}\text{Fe}_{0.5}\text{O}_{5+\delta}$) cobaltites; the thermal expansion coefficients of the latter are much higher, falling in a range of $(15\text{--}30)\cdot 10^{-6} \text{ K}^{-1}$ [32]. Along with desirable thermal functions, the total conductivity of LNF attains $200\text{--}1000 \text{ S cm}^{-1}$ depending on the iron/nickel ratio [33]; this allows such materials to be utilized as current collectors instead of the Pt electrodes or as an electronic component of composite materials [31,34]. However, electrochemical performance of the LNF electrodes is insufficient [35], since they exhibit predominantly electronic behavior instead of mixed ionic–electronic conduction; this fact can be explained by a low oxygen deficiency variation in LNF ($3-\delta \approx 3$) that provides a negligible amount of oxygen vacancies and, correspondingly, low oxygen-ionic conductivity. By replacing lanthanum in LaNiO_3 with a more redox active element (praseodymium), coupled with a further doping with transition elements (iron or cobalt), it is possible to tailor the defect structure and functional properties of the obtained phases for designing compatible and high-performance electrodes for PCFC applications.

2. Materials and Methods

2.1. Materials Preparation

Materials of $\text{PrNi}_{0.4}\text{Fe}_{0.6}\text{O}_{3-\delta}$ (PNF) and $\text{PrNi}_{0.4}\text{Co}_{0.6}\text{O}_{3-\delta}$ (PNC) compositions were synthesized via the citrate–nitrate method using nitrates of the corresponding metals: $\text{Pr}(\text{NO}_3)_3$, $\text{Ni}(\text{NO}_3)_2$, $\text{Fe}(\text{NO}_3)_3$ and $\text{Co}(\text{NO}_3)_3$. Stoichiometric amounts of the precursors were dissolved in distilled water, and then citric acid was added to the homogeneous melt. The molar ratio between the total number of metal cations and citric acid was 1:2. During heating to $320 \text{ }^\circ\text{C}$, the obtained solution transformed into a transparent gel and then self-ignited. The formed black colored powder materials were subjected to thermal treatment at $1000 \text{ }^\circ\text{C}$ for 5 h to remove any organic traces. Then, the powders were ground in acetone in a Fritsch Pulverisette 7 planetary mill (Fritsch, Germany) at a frequency of 350 rpm for 1 h. In order to obtain the desired composition, the powders were compacted and calcined at $1200 \text{ }^\circ\text{C}$ for 5 h. Next, the samples were analogously ground and pressed into pellets using a hydraulic press with a force of 3 tonnes. The relative density of the resultant ceramic materials exceeded 95% of the theoretical density.

To prepare single electrochemical cells, $\text{BaCe}_{0.6}\text{Zr}_{0.2}\text{Y}_{0.2}\text{O}_{3-\delta}$ (BCZY) and $\text{Ce}_{0.9}\text{Gd}_{0.1}\text{O}_{2-\delta}$ (CGO) electrolyte materials were synthesized by nitrate–citrate auto-combustion technique. Here, nitrates of the corresponding elements served as precursors and citric acid was used as a fuel. The powdered BCZY and CGO materials were synthesized at $1150 \text{ }^\circ\text{C}$ and $1100 \text{ }^\circ\text{C}$ for 5 h, respectively. The oxygen-ionic (ZrO_2)_{0.92}(Y_2O_3)_{0.08} (YSZ) electrolyte was prepared in the same way, but with two calcination steps (1000 and $1100 \text{ }^\circ\text{C}$ for 5 h).

2.2. Characterization of Materials

The phase composition and crystalline structure of the obtained powders and ceramic samples was studied by X-ray diffraction analysis using a D/MAX-2200 diffractometer

(Rigaku Co. Ltd., Japan) in $\text{CuK}\alpha$ emission at a wavelength of $\lambda = 1.54056 \text{ \AA}$ with an angular range of $20^\circ \leq 2\theta \leq 80^\circ$. The Inorganic Crystal Structure Database (ICSD) was used to determine the initial phase composition. Then, in order to specify the structural parameter, the XRD data were analyzed using the Rietveld method [36] via FullProf program software [37].

The cross-sectional morphology and elemental composition of the single electrochemical cells was characterized by the scanning electron microscopy (SEM) analysis using a Phenom ProX electron microscope (Thermo Fisher Scientific, USA). The images of the surfaces of the studied materials were obtained under back electron scattering (BES) regime with an accelerating voltage of 15 kV.

The chemical interaction between PNF and PNC electrode materials with $\text{BaCe}_{0.6}\text{Zr}_{0.2}\text{Y}_{0.2}\text{O}_{3-\delta}$, $\text{Ce}_{0.9}\text{Gd}_{0.1}\text{O}_{2-\delta}$ or YSZ electrolytes was studied by mixing them in a ratio of 50:50 wt%. The obtained mixtures were calcined at 1100°C for 10 h. The presence and composition of the products of chemical interaction were determined by XRD analysis.

The thermomechanical behavior of the electrode materials under heating/cooling modes was studied using a Netzsch DIL 402 C dilatometer (Netzsch, Germany). The measurements were performed in air within a temperature range of $50\text{--}1000^\circ\text{C}$ at a constant heating/cooling rate of 3°C min^{-1} . The linear thermal expansion coefficient values were determined on linear regions of the dilatometry curves.

The electrical conductivity of electrode materials was analyzed using the four-probe DC method at temperatures ranging from 20 to 900°C . The measurements were performed under cooling mode after 50°C and 1 h isothermal exposure at each step. In order to provide the necessary contact when measuring electrical conductivity, Pt electrodes were used.

2.3. Electrochemical Behavior of $\text{PrNi}_{0.4}\text{Fe}_{0.6}\text{O}_{3-\delta}$ and $\text{PrNi}_{0.4}\text{Co}_{0.6}\text{O}_{3-\delta}$ Electrodes

The electrolyte of the $\text{BaCe}_{0.6}\text{Zr}_{0.2}\text{Y}_{0.2}\text{O}_{3-\delta}$ composition preliminarily annealed at 1430°C for 5 h served as a basis for the fabrication of symmetrical cells. The PNF/PNC electrode ink was prepared as follows: the corresponding electrode powder was first ground in a Fritsch Pulverisette 7 planetary mill at 550 rpm for 1 h. Then, a mixture of α -terpineol, ethyl cellulose, and dibutyl phthalate was added to the powder to serve as an organic binder; these components were then mixed in ethyl propylene alcohol. After applying the electrodes to the opposite surfaces of the electrolyte via the airbrush coating method, the cell was sintered at 1000°C for 1 h.

The obtained symmetrical cells were electrochemically characterized using a Amel 2550 high-current potentiostat–galvanostat (Amel, Italy) with a Materials M520 frequency response analyzer (MaterialsM, Italy) in the temperature range of $400\text{--}800^\circ\text{C}$ in humid air ($p\text{H}_2\text{O} = 0.03 \text{ atm}$) at frequencies ranging from 1×10^{-2} to $1 \times 10^6 \text{ Hz}$ and a voltage amplitude of 50 mV. The data were obtained in cooling mode. The experimental spectra fitting was performed by means of the equivalent circuit method using ZView software, Scribner Associates Inc. [38].

3. Results and Discussion

3.1. Phase Structure and Chemical Compatibility

Single-phase materials of the PNF and PNC compositions were obtained using the citrate–nitrate synthesis method. Figure 1 illustrates X-ray diffraction patterns of the studied samples processed by means of the Rietveld refinement. It can be seen that the experimental data agree well with the calculated equivalents. All diffraction peaks are indexable within an orthorhombic perovskite structure described by the Pbnm space group. The refinement parameters of the unit cell for the PNF sample are as follows: $a = 5.5013 \text{ \AA}$, $b = 7.7309 \text{ \AA}$, $c = 5.4539 \text{ \AA}$, and $V = 231.9 \text{ \AA}^3$. The equivalent parameters for the PNC sample are $a = 5.3764 \text{ \AA}$, $b = 7.6110 \text{ \AA}$, $c = 5.3885 \text{ \AA}$, and $V = 220.5 \text{ \AA}^3$.

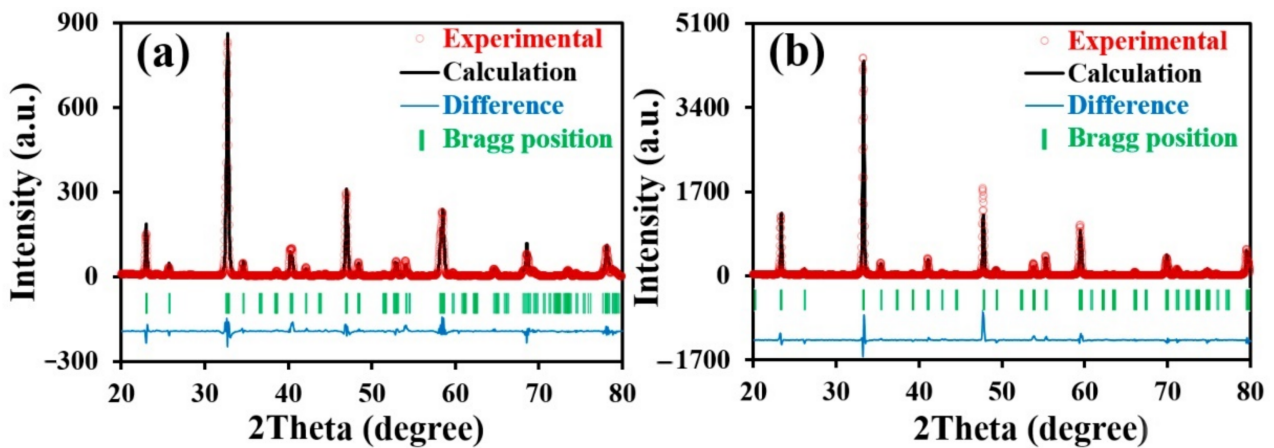


Figure 1. Rietveld refinement results for the $\text{PrNi}_{0.4}\text{Fe}_{0.6}\text{O}_{3-\delta}$ (a) and $\text{PrNi}_{0.4}\text{Co}_{0.6}\text{O}_{3-\delta}$ (b) at room temperature.

To provide long-term stability, SOFC material components should have good chemical compatibility. Therefore, the chemical compatibility of the PNF and PNC electrode materials was studied with promising BCZY, CGO, and YSZ electrolytes by mixing the corresponding powders and calcinating them at $1100\text{ }^{\circ}\text{C}$ for 10 h. The X-ray diffraction patterns for these calcined mixtures are depicted in Figure 2.

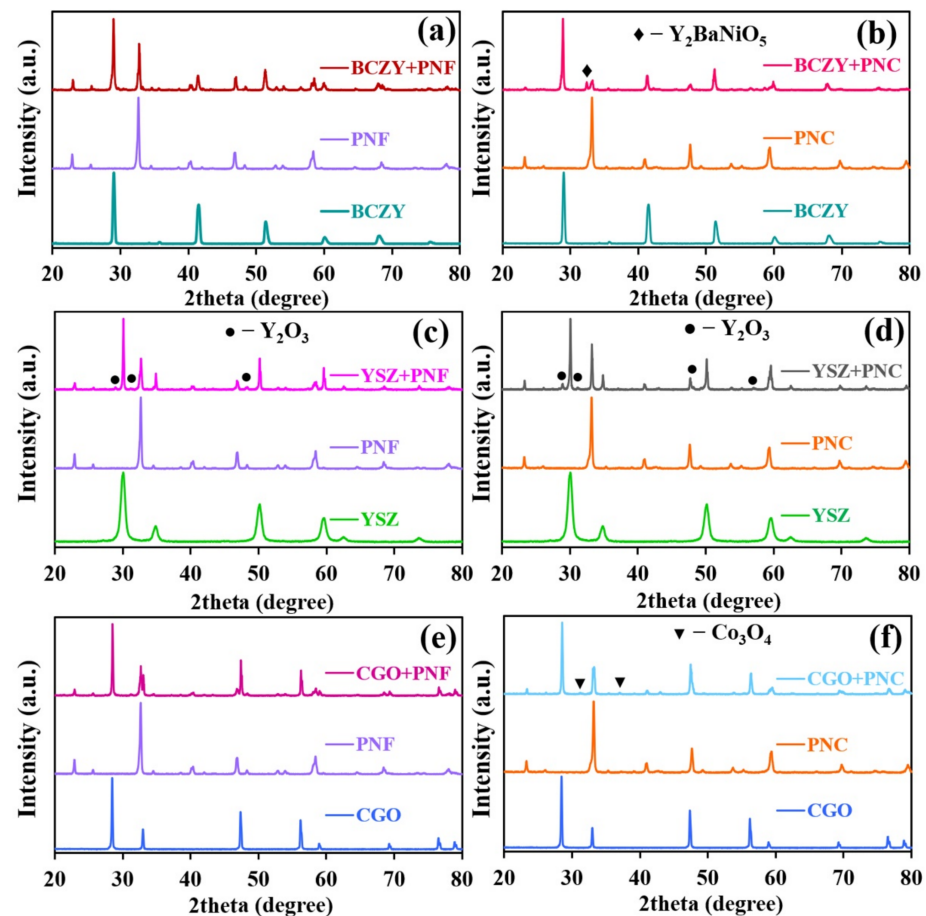


Figure 2. XRD patterns of the $\text{PrNi}_{0.4}\text{Fe}_{0.6}\text{O}_{3-\delta}$ (a,c,e) or $\text{PrNi}_{0.4}\text{Co}_{0.6}\text{O}_{3-\delta}$ (b,d,f) with BCZY (a,b), YSZ (c,d), and CGO (e,f) powders after treatment at $1100\text{ }^{\circ}\text{C}$ for 10 h.

It was found that the cobalt-containing electrode has low chemical compatibility with all the proposed electrolytes. In detail, the interaction of BCZY with PNC leads to an Y_2BaNiO_5 impurity phase, which tends to be localized at the grain boundaries of the electrolyte, leading to considerable ionic transport degradation across the grain boundaries [39,40]. In addition, a significant decrease in the content of the PNC phase in its mixture with the BCZY phase is distinguished. This may be due to a significant decomposition of the initial PNC phase whose cations go to the composition of Y_2BaNiO_5 impurity, such as $\text{Pr}_2\text{Ba}(\text{Ni},\text{Co},\text{Y})\text{O}_5$ [41]. In addition, the intensity of reflexes for the PNC phase is also quite small. Therefore, one can conclude that most of the cations were embedded into the BCZY structure, since the Pr [42], Ni [43], and Co [44] cations can be indeed incorporated in the cerium/irconium position. Another possible explanation relies on the assumption that some phases, such as NiO , Co_3O_4 , Pr_6O_{11} , and Y_2O_3 , can be localized at an intergrain region. In this case, when they are evenly separated, they become difficult to be detected with XRD.

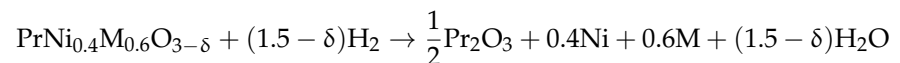
It is noteworthy that no such interaction occurs in the case of PNF. The chemical reaction occurring between PNC cathodes and YSZ or CGO electrolytes was found to result in the formation of additional Y_2O_3 and Co_3O_4 impurities along with the basic phases.

The obtained iron-containing nickelate is characterized by its higher chemical stability. Trace amounts of the undesirable yttrium oxide phase are observed in the interaction of the electrolyte with the YSZ-based electrolyte, while other mixtures are relatively stable in terms of forming any impurities, at least at detectable amounts.

3.2. Thermal Properties

The absolute oxygen content of the complex oxides was calculated using thermogravimetric analysis (TGA) in pure hydrogen medium when heated to 1000 °C. In order to remove adsorbed gases and moisture, the samples were pre-calcined in air at 1000 °C for 4 h.

It has been assumed that the samples are reduced in hydrogen according to the following reaction:



The released water is removed by gas flow, during which process the samples are observed to undergo weight loss (Figure 3a). On the basis of these changes, the oxygen content of the samples was estimated (Figure 3b): the absolute oxygen content at room temperatures were 2.89 and 2.93 for the Fe- and Co-containing samples, respectively.

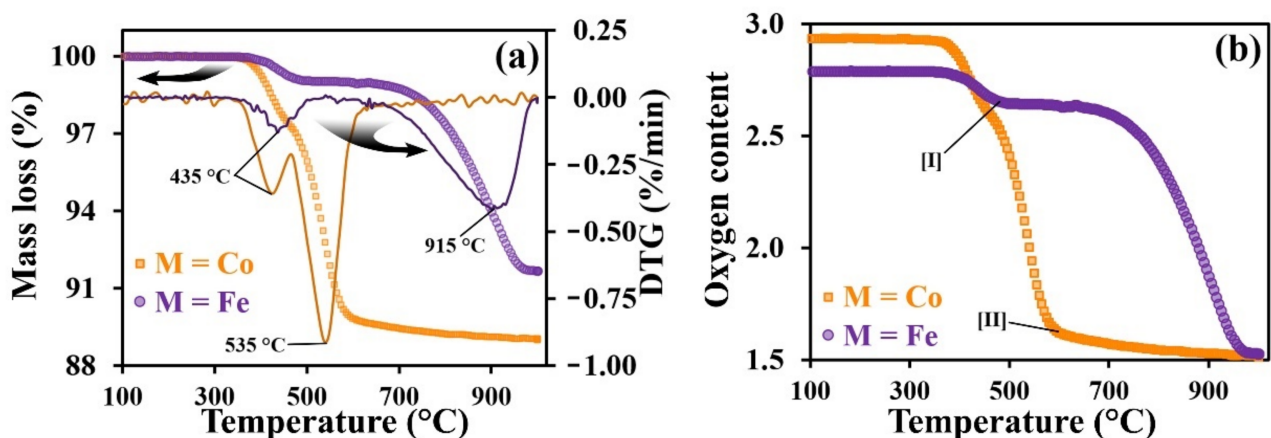


Figure 3. Thermogravimetric data of the $\text{PrNi}_{0.4}\text{Fe}_{0.6}\text{O}_{3-\delta}$ and $\text{PrNi}_{0.4}\text{Co}_{0.6}\text{O}_{3-\delta}$ powders: TGA and DTG data (a) and oxygen content in oxides during reduction in H_2 (b).

On the differential TGA data, there are a number of characteristic peaks (Figure 3a). Similarly, several regions can be distinguished in the temperature dependence of oxygen content (Figure 3b), in which the active processes in the samples are terminated. These are designated as [I] for the Fe-based sample at ~ 500 °C and [II] for the Co-based sample at ~ 600 °C. The peak at 435 °C indicates a sharp decrease in weight of both samples; for the PNC, this process is terminated, as shown by point [III]. It is most likely that this weight loss is due to the nickel reduction. The peak at 535 °C was observed for the Co-containing sample, and the oxygen content at point [III] was about 1.67. However, since no further weight loss was detected, this process associated with peak at 565 °C can represent the complete reduction of cobalt-ions to a metallic state. The peak at 915 °C represents the weight loss during the iron reduction. After these processes have been completed, a slow weight reduction to a stable value was observed, indicating the full reduction of the remaining nickel, cobalt, and iron cations.

3.3. Thermal Expansion Behavior

The thermal expansion coefficient (TEC) comprises a basic parameter for SOFC components. Any difference in TEC values between the cathode and electrolyte may result in significant deformations following thermal cycling, which leads to cracking and delamination of components. The TEC values of the studied materials were determined via the dilatometry method. Figure 4a illustrates the temperature dependencies of the relative linear size changes, which were measured at heating from room temperature to 1000 °C.

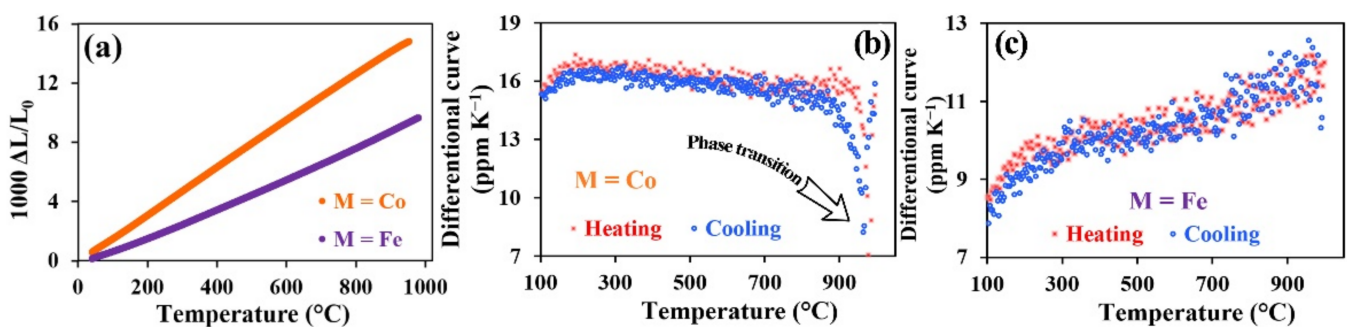


Figure 4. Dilatometry data of the ceramic $\text{PrNi}_{0.4}\text{M}_{0.6}\text{O}_{3-\delta}$ samples: temperature dependence of linear expansion at the cooling (a) and differential TEC values (b,c) obtained at the heating and cooling.

Figure 4b illustrates differential curves of the dilatometry data for PNC, which clearly show a rapid decrease in TEC values at 950 °C for both cooling and heating. This behavior, according to literature data, is related to a phase transition that occurs due to structural change from orthorhombic to tetragonal lattice symmetry [45]. Apart from that, the lattice expansion, which is observed at elevated temperatures, may be associated with the loss of oxygen in the lattice and consequent formation of oxygen vacancies. The appearance of oxygen vacancies accompanied with the thermal reduction of Co^{4+} , Co^{3+} , and Ni^{3+} cations to the lower valence states results in the increased inflexion of the thermal expansion curves observed at high temperatures. Since the presence of unstable nickel cations in these oxides is unlikely, it is considered that only cobalt ions are affected by the above-described mechanism [46].

The TEC values calculated using the linear regions of the curves in low-temperature and high-temperature intervals are presented in Table 1.

Table 1. Low-temperature, high-temperature, and average TEC values of $\text{PrNi}_{0.4}\text{M}_{0.6}\text{O}_{3-\delta}$ determined within various temperature ranges and regimes.

| Composition | Heating | | | | Cooling | | | |
|-------------|---------|--------|---------|----------|---------|--------|---------|----------|
| | T* | 100–T* | T*–1000 | 100–1000 | T* | 100–T* | T*–1000 | 100–1000 |
| M = Co | 580 | 16.5 | 15.5 | 16.0 | 550 | 16.1 | 15.2 | 15.7 |
| M = Fe | 620 | 9.9 | 10.5 | 10.2 | 630 | 9.6 | 11.1 | 10.4 |

In the case of $\text{PrNi}_{0.4}\text{Fe}_{0.6}\text{O}_{3-\delta}$, the differential curve (Figure 4c) is convex both before and after the inflexion point (T*). There is a significant difference between the TEC values of iron- and cobalt-containing samples. At temperatures exceeding T*, a chemical expansion effect due to partial iron and nickel reduction processes co-exists along with the dominating thermal expansion. The linear expansion of the samples is associated with the increase in elementary cell volume, which is caused by changes in the ionic radii of iron (from 0.645 Å (HS) for Fe^{+3} or 0.80 Å for Fe^{2+}) and nickel (from 0.6 Å (HS) or 0.56 Å (LS) for Ni^{+3} to 0.69 Å for Ni^{2+}) cations [47]. The average TEC value for $\text{PrNi}_{0.4}\text{Fe}_{0.6}\text{O}_{3-\delta}$ is equal to $10.2 \cdot 10^{-6} \text{ K}^{-1}$. We note that high-temperature modification of the composition with iron demonstrates a higher TEC value than that obtained from low-temperature modification. A phase transition from orthorhombic to rhombohedral structure may also occur in the temperature interval of the curve break—for example, in $\text{LaNi}_{0.4}\text{Fe}_{0.6}\text{O}_3$ and $\text{LaNi}_{0.2}\text{Fe}_{0.8}\text{O}_{3-\delta}$ [48].

Table 2 illustrates a comparative analysis of the average TEC values of $\text{PrNi}_{0.4}\text{M}_{0.6}\text{O}_{3-\delta}$ and those associated with the most frequently used nickel and praseodymium-based cathode materials [46,49–53]. It was found that the TEC values of the studied materials correspond with the TEC values of other cathode materials. This fact has a favorable effect on the adhesion and thermal compatibility of the studied samples when used as electrolyte materials and makes them attractive for the relevant electrochemical applications. In particular, the TEC values of the studied materials are close to those of the most frequently used electrolyte materials: YSZ ($11 \cdot 10^{-6} \text{ K}^{-1}$ [54]), $\text{BaCe}_{0.8}\text{Y}_{0.2}\text{O}_{3-\delta}$ ($11.6 \cdot 10^{-6} \text{ K}^{-1}$ [55]), and $\text{Ce}_{0.9}\text{Gd}_{0.1}\text{O}_{2-\delta}$ ($12.0 \cdot 10^{-6} \text{ K}^{-1}$ [56]).

Table 2. Comparative analysis of the TEC values for Pr- and Ni-containing cathode materials.

| Composition | Temperature Interval, °C | TEC · 10 ⁶ , K ^{−1} | References |
|---|--------------------------|---|------------|
| $\text{PrNi}_{0.4}\text{Fe}_{0.6}\text{O}_{3-\delta}$ | 100–1000 | 10.4 | This work |
| $\text{PrNi}_{0.4}\text{Co}_{0.6}\text{O}_{3-\delta}$ | | 15.7 | |
| $\text{PrNiO}_{3-\delta}$ | 25–1000 | 12.7 | [49] |
| $\text{PrFe}_{0.7}\text{Ni}_{0.3}\text{O}_{3-\delta}$ | 25–900 | 8.4–11.0 | [50] |
| $\text{PrNi}_{0.4}\text{Fe}_{0.6}\text{O}_{3-\delta}$ | 400–800 | 10.5–11.4 | [51] |
| $\text{Pr}_{0.7}\text{Sr}_{0.3}\text{Fe}_{0.6}\text{Ni}_{0.4}\text{O}_{3-\delta}$ | 25–1000 | 14.1 | [52] |
| $\text{Pr}_{0.7}\text{Sr}_{0.3}\text{Fe}_{0.5}\text{Ni}_{0.5}\text{O}_{3-\delta}$ | 25–1000 | 13.5 | [52] |
| $\text{Pr}_{0.5}\text{Sr}_{0.5}\text{Co}_{0.6}\text{Ni}_{0.4}\text{O}_{3-\delta}$ | 100–255 | 15.7 | [46] |
| | 400–800 | 21.6 | |
| | 800–1000 | 27.5 | |
| $\text{La}_{0.9}\text{Sr}_{0.1}\text{Fe}_{0.6}\text{Ni}_{0.4}\text{O}_{3-\delta}$ | 420–700 | 12.2 | [53] |
| | 700–1150 | 13.1 | |

Thus, the dilatometric curve form for the studied samples is explained by the mutual influence of the chemical expansion and changes in the phase structure of the materials.

3.4. Total Conductivity

The high electrical conductivity of the studied materials supports effective electron transfer, which is one of the key factors for their application as SOFC cathodes. The

electrical conductivity of sintered samples was studied using the four-probe DC method in the temperature range of 50–900 °C (Figure 5).

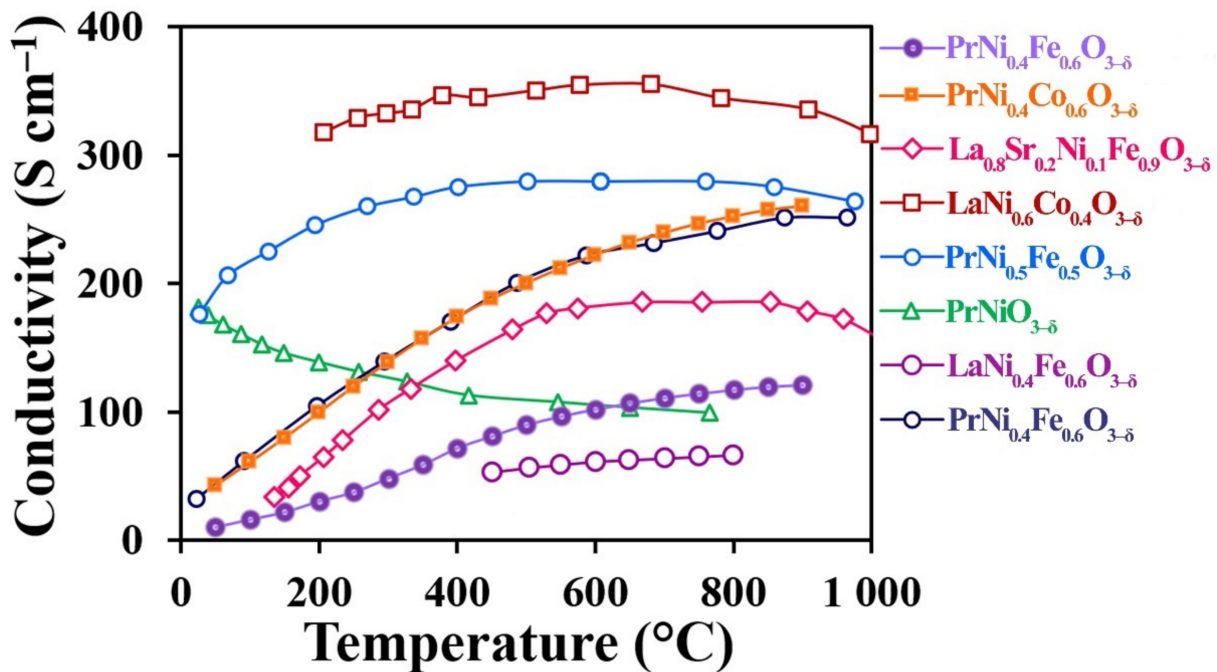


Figure 5. Electrical conductivity of the $\text{PrNi}_{0.4}\text{Fe}_{0.6}\text{O}_{3-\delta}$ and $\text{PrNi}_{0.4}\text{Co}_{0.6}\text{O}_{3-\delta}$ materials compared with electrical conductivities of $\text{LaNi}_{0.6}\text{Co}_{0.4}\text{O}_{3-\delta}$ [57], $\text{PrNi}_{0.5}\text{Fe}_{0.5}\text{O}_{3-\delta}$ [58], $\text{La}_{0.8}\text{Sr}_{0.2}\text{Ni}_{0.1}\text{Fe}_{0.9}\text{O}_{3-\delta}$ [53], $\text{PrNiO}_{3-\delta}$ [49], $\text{LaNi}_{0.4}\text{Fe}_{0.6}\text{O}_{3-\delta}$ [59], and $\text{PrNi}_{0.4}\text{Fe}_{0.6}\text{O}_{3-\delta}$ [60].

The increasing temperature dependence of the electrical conductivity testifies to the semi-conductive character of the studied materials. Their electrical conductivity may be described by the model of hopping conductivity of small radii polarons according to the equation:

$$\sigma = \frac{A}{T} \exp\left(-\frac{E_a}{kT}\right), \quad (1)$$

where A is the pre-exponential multiplier, S cm^{-1} , T is the absolute temperature, K , k is the Boltzmann constant, and E_a is the activation energy. The activation energy values were calculated using the temperature dependence linear regions of the total conductivity. The obtained E_a values are nearly the same for the studied temperatures. Thus, for $M = \text{Fe}$ and $M = \text{Co}$, the E_a total conductivity values are 0.27 and 0.32 eV, respectively. Such activation energy values correspond to those of the charge transfer energy barrier according to the small polaron hopping mechanism.

Figure 5 presents the electrical conductivity temperature dependencies for the frequently used electrode materials. It is interesting to note that, according to the literature data, the electrical conductivity of the undoped praseodymium nickelate has a primarily metallic character.

The electrical conductivity values obtained for $\text{PrNi}_{0.4}\text{Fe}_{0.6}\text{O}_{3-\delta}$ and $\text{PrNi}_{0.4}\text{Co}_{0.6}\text{O}_{3-\delta}$ at 600 °C are 102 and 222 S cm^{-1} , respectively, demonstrating that the studied materials are promising for use in SOFC cathodes.

3.5. Electrochemical Characterization

In order to evaluate the $\text{PrNi}_{0.4}\text{Fe}_{0.6}\text{O}_{3-\delta}$ and $\text{PrNi}_{0.4}\text{Co}_{0.6}\text{O}_{3-\delta}$ electrochemical activity, we fabricated symmetrical cells based on the BCZY electrolyte. Due to the microstructure of the electrodes having a significant influence on their electrochemical behavior, we performed SEM analysis of their cross sections prior to characterizing the cells (Figure 6). It is shown that the BCZY electrolyte is dense, and the electrode materials are well-adhered.

The formed electrodes have different structural parameters (particle size and porosity). Both factors have a significant impact on the polarization characteristics of these materials.

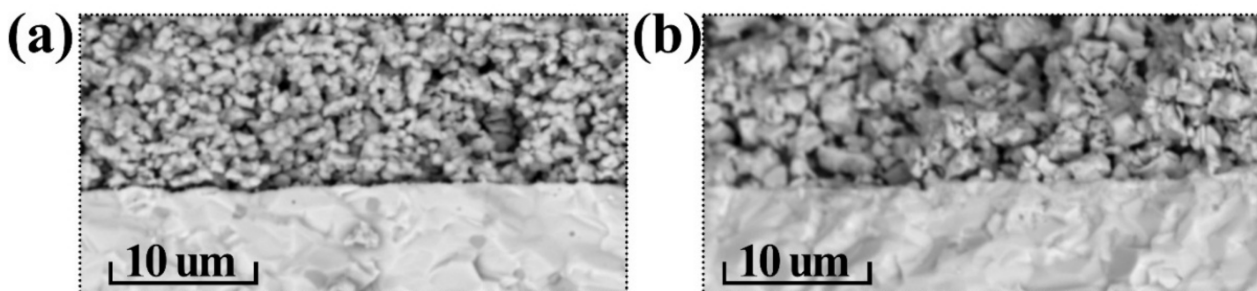


Figure 6. SEM analysis of the $\text{PrNi}_{0.4}\text{M}_{0.6}\text{O}_{3-\delta} | \text{BaCe}_{0.6}\text{Zr}_{0.2}\text{Y}_{0.2}\text{O}_{3-\delta}$ interfaces for the prepared symmetrical cells: M = Fe (a) and M = Co (b).

The obtained electrochemical impedance spectroscopy (EIS) spectra are illustrated in Figure 7. There is a noticeable difference between the impedance spectra profiles. That is why different electrochemical models with equivalent schemes were used to process the obtained impedance spectra for Me = Fe and Co. The resistor model imitating the ohmic electrolyte resistance, and L induction, imitating the frequency reaction of the measurement cell current leads, were used for both samples. The impedance of the Fe-containing sample was fitted using two subsequent R-CPE chains. Regarding the Co-containing sample, a distributed element (DE) applied in the Addler model was used along with two downstream R-CPE chains. The Havriliak–Negami DE impedance is described by the following equation:

$$Z_{\text{DE}}(\omega) = \frac{R_{\text{chem}}}{(1 + (i\omega\tau_{\text{chem}})^{\alpha})^{\varphi}} \quad (2)$$

where R_{chem} is the resistance of the system associated with the difficulty of current flow during the electrochemical reaction in the porous electrode, and τ_{chem} can be regarded as the time constant of the element. At the limiting value of $\alpha = 1$, τ_{chem} is equivalent to the cell capacity. In the used model, $\alpha \rightarrow 1$ and $\varphi \sim 0.5$, which brings the applied DE closer to the Gehrisher element. Figure 8 illustrates the models and spectra of the elements. The performed data fitting is used to obtain partial polarization resistance values of symmetrical cells (Figure 9).

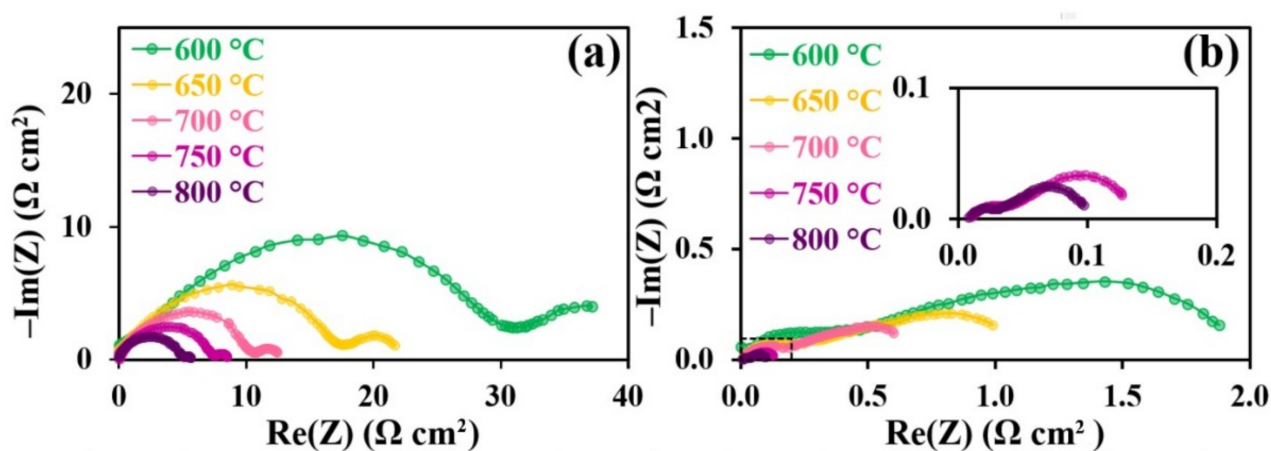


Figure 7. Electrochemical data obtained for the PNF | BCZY | PNF (a) and PNC | BCZY | PNC (b) symmetrical cells.

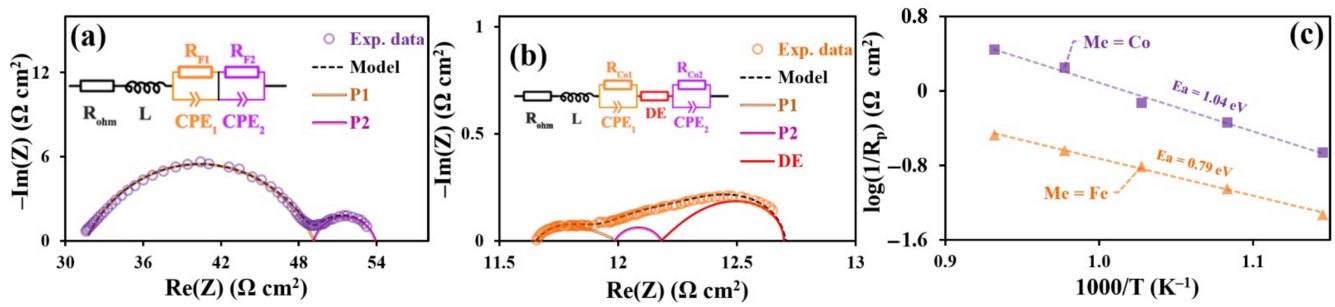


Figure 8. Fitting impedance data of symmetry cells with the $\text{PrNi}_{0.4}\text{Fe}_{0.6}\text{O}_{3-\delta}$ and $\text{PrNi}_{0.4}\text{Co}_{0.6}\text{O}_{3-\delta}$ electrodes: used models for fitting impedance data of cells with Fe (a) and Co-contended (b) air electrodes and temperature dependencies of polarization resistance these cells (c).

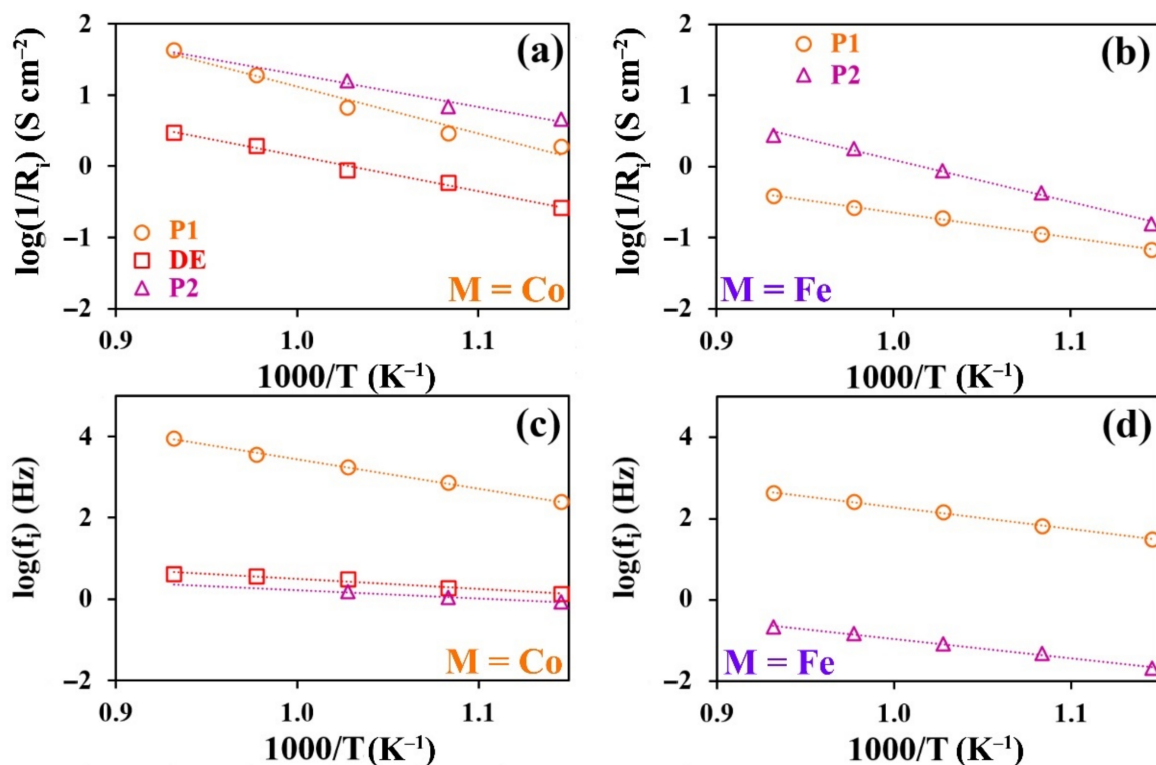


Figure 9. Partial values of the polarization resistances (a,b) and frequencies (c,d), determined by fitting of impedance spectra, corresponding to the electrode processes in symmetrical cells for $\text{PNC}|\text{BCZY}|\text{PNC}$ (a,c) and $\text{PNF}|\text{BCZY}|\text{PNF}$ (b,d).

For both systems, the P_1 process is characterized by the capacity in the range from 1 to $7 \cdot 10^{-4} \text{ F} \cdot \text{cm}^2$, which is characteristic for the flow of H^+ and O^{2-} ions through the electrode/electrolyte interface [61]. The activation energy values of the polarization resistance calculated from the Arrhenius dependencies were 0.7 and 1.3 eV for Fe- and Co-containing samples, respectively. In the case of the Fe-containing material, the P_1 process undoubtedly influences the charge transfer through the electrode/electrolyte interface. However, the relatively high activation energy of the polarization conductivity of Co-containing electrodes calls the nature of this process into question. Such activation energy and capacity values were observed for the flow processes of oxygen ions through the electrolyte bulk [62]. Since the process capacities are very similar for both samples, we may conclude that P_1 is a complex process: the transfer of charge through the electrode/electrolyte interface influences the polarization resistance in the Fe-containing samples, while the polarization process in the Co-containing samples is influenced by the transfer of ions to the electrode

volume. The polarization resistance of the symmetrical cell with Fe-containing electrodes significantly exceeds that of the symmetrical cells with Co-containing electrodes. This fact may be associated with the lower conductivity of the Fe-containing nickelate (Figure 5), which is reflected in the processes at the three-phase electrode/electrolyte/air boundary. Another explanation for the difference in P_1 activation energies between the electrochemical cells with Fe- and Co-containing electrodes is the possible appearance of a small amount of the Y_2BaNiO_5 phase (Figure 2b). Given the available data on this phase [63], it is reasonable to conclude that its presence is undesirable and may lead to partial blocking of ion transfer across the interface, leading to an increase in the P_1 activation energy.

The P_2 process is characterized by capacities in the range of 0.8–2.0 F·cm² and activation energies of 1.17 and 0.90 eV for the Fe- and Co-containing samples, respectively. The very high observed capacity values are difficult to be associated with the electrochemical nature of the process. In addition, the closeness of the activation energy and capacity values for both cells denotes the common nature of the processes. The nature of the processes may be associated with oxygen adsorption–desorption occurring at the electrode surfaces [64]. The decrease in partial polarization resistance P_2 observed for the PNC samples, may be caused by the microstructural peculiarities of the material.

Considering the model used, in which DE is analogous to the Gehrisher element, the distributed element process can be related to redox processes in the porous electrodes. The fact that the DE process was not observed for the Fe-containing samples may be explained by the relatively low resistance values as compared to other Fe electrode processes.

Table 3 provides a comparative analysis of the polarization resistance values of symmetrical cells having $PrNi_{0.4}M_{0.6}O_{3-\delta}$ electrodes, where $M = Fe, Co$ and their analogues. Although the comparison is limited by a lack of data for proton-conducting electrolytes among the presented studied materials, the missing values should not differ greatly from those illustrated. It is seen that the polarization resistance values of the studied materials correlated well with their analogues; this is especially characteristic for the co-doped nickelate, which has the smallest polarization resistance value at the studied temperatures.

Table 3. Polarization resistance values of symmetrical cells with $PrNiO_3$ -based electrodes.

| Electrode | Electrolyte | $R_p, \Omega \text{ cm}^2$ | | References |
|--|--|----------------------------|--------|------------|
| | | 600 °C | 700 °C | |
| $PrNi_{0.4}Fe_{0.6}O_{3-\delta}$ | BCZY | 21.1 | 6.46 | This work |
| $PrNi_{0.4}Co_{0.6}O_{3-\delta}$ | | 4.6 | 1.3 | |
| $PrNiO_{3-\delta}$ | | 0.91 | 0.13 | [49] |
| $Pr_{0.7}Sr_{0.3}Fe_{0.6}Ni_{0.4}O_{3-\delta}$ | | 40.9 | 4.7 | [52] |
| $PrFe_{0.6}Ni_{0.4}O_{3-\delta}$ | $Ce_{0.9}Gd_{0.1}O_{2-\delta}$ | 20.1 | 2.5 | [60] |
| $PrFe_{0.5}Ni_{0.5}O_{3-\delta}$ | | 17.8 | 1.4 | |
| $PrFe_{0.4}Ni_{0.6}O_{3-\delta}$ | | 24.6 | 2.8 | |
| $LaFe_{0.4}Ni_{0.6}O_{3-\delta}$ | | 3.5 | 0.4 | |
| $PrNi_{0.6}Co_{0.4}O_{3-\delta}$ | $Ce_{0.8}Sm_{0.2}O_{2-\delta}$ | 0.7 | 0.1 | [65] |
| $LaNi_{0.6}Co_{0.4}O_{3-\delta}$ | $La_{0.8}Sr_{0.2}Ga_{0.83}Mg_{0.17}O_{3-\delta}$ | 34.0 | 2.9 | [66] |
| $LaNi_{0.6}Fe_{0.4}O_{3-\delta}$ | $La_{0.8}Sr_{0.2}Ga_{0.83}Mg_{0.17}O_{3-\delta}$ | 27.3 | 3.2 | |
| $LaNi_{0.6}Fe_{0.4}O_{3-\delta}$ | YSZ | 373.2 | 81.9 | [67] |
| $LaNi_{0.6}Fe_{0.4}O_{3-\delta}$ | $Ce_{0.8}Gd_{0.2}O_{2-\delta}$ | 3.3 | 0.4 | [68] |
| $LaNi_{0.6}Fe_{0.4}O_{3-\delta}$ | $Ce_{0.9}Gd_{0.1}O_{2-\delta}$ | 21.4 | 2.7 | [69] |
| $LaNi_{0.4}Co_{0.6}O_{3-\delta}$ | YSZ | 0.1 | 0.04 | [70] |
| $LaCo_{0.6}Ni_{0.4}O_{3-\delta}$ | $Ce_{0.8}Gd_{0.2}O_{2-\delta}$ | 326.0 | 45.0 | [71] |
| $LaNi_{0.6}Fe_{0.4}O_{3-\delta}$ | $Ce_{0.8}Sm_{0.2}O_{2-\delta}$ | 7.6 | 1.2 | [72] |

4. Conclusions

The present work provides a comprehensive analysis of the $\text{PrNi}_{0.4}\text{Fe}_{0.6}\text{O}_{3-\delta}$ and $\text{PrNi}_{0.4}\text{Co}_{0.6}\text{O}_{3-\delta}$ complex oxides, which are attractive for application as oxygen electrodes for protonic ceramic fuel cells. These phases were successfully obtained by the citrate-nitrate combustion method followed by high-temperature synthesis. The single-phase powder and ceramic materials were shown to possess certain advantages in their functional properties. On the one hand, Fe-containing samples show good thermal/chemical compatibility with protonic-conducting electrolytes. For example, the average thermal expansion coefficient value of $\text{PrNi}_{0.4}\text{Fe}_{0.6}\text{O}_{3-\delta}$ is considerably lower than that of $\text{PrNi}_{0.4}\text{Co}_{0.6}\text{O}_{3-\delta}$ (10.4 and $15.7 \cdot 10^{-6} \cdot \text{K}^{-1}$, respectively). On the other hand, high conductivity and good electrochemical behavior are observed for the Co-containing nickelate (at $600 \text{ }^\circ\text{C}$, 222 S cm^{-1} , and $4.6 \text{ } \Omega \text{ cm}^2$, respectively) compared to its Fe-based counterpart (102 S cm^{-1} and $21.1 \text{ } \Omega \text{ cm}^2$, respectively). However, both studied materials also demonstrated certain disadvantages, which require further study for improvement of these functions.

Author Contributions: Conceptualization, D.A.M.; methodology, G.K.V. and A.P.T.; software, A.P.T.; validation, A.V.K., J.G.L. and A.P.T.; formal analysis, D.A.M.; investigation, A.V.K., J.G.L. and A.P.T.; data curation, D.A.M.; writing—original draft preparation, A.P.T., A.V.K. and D.A.M.; writing—review and editing, D.A.M.; visualization, A.P.T. and A.V.K.; supervision, D.A.M.; project administration, D.A.M. All authors have read and agreed to the published version of the manuscript.

Funding: This research received no external funding.

Institutional Review Board Statement: Not applicable.

Informed Consent Statement: Not applicable.

Data Availability Statement: Data is contained within the article.

Acknowledgments: The characterization of powder and ceramic materials was carried out at the Shared Access Centre “Composition of Compounds” of Institute of High-Temperature Electrochemistry (Ekaterinburg, Russia). We would like to give a special thanks to Natalia Popova and Thomas Beavitt for the performed proofreading [73].

Conflicts of Interest: The authors declare no conflict of interest.

References

1. Noussan, M.; Raimondi, P.P.; Scita, R.; Hafner, M. The role of green and blue hydrogen in the energy transition—A technological and geopolitical perspective. *Sustainability* **2020**, *13*, 298. [[CrossRef](#)]
2. Yue, M.; Lambert, H.; Pahon, E.; Roche, R.; Jemei, S.; Hissel, D. Hydrogen energy systems: A critical review of technologies, applications, trends and challenges. *Renew. Sustain. Energy Rev.* **2021**, *146*, 111180. [[CrossRef](#)]
3. Oliveira, A.M.; Beswick, R.R.; Yan, Y. A green hydrogen economy for a renewable energy society. *Curr. Opin. Chem. Eng.* **2021**, *33*, 100701. [[CrossRef](#)]
4. Aditiya, H.B.; Aziz, M. Prospect of hydrogen energy in Asia-Pacific: A perspective review on techno-socio-economy nexus. *Int. J. Hydrog. Energy* **2021**, *46*, 35027–35056. [[CrossRef](#)]
5. Ahmad, M.S.; Ali, M.S.; Rahim, N.A. Hydrogen energy vision 2060: Hydrogen as energy carrier in Malaysian primary energy mix—Developing P2G case. *Energy Strat. Rev.* **2021**, *35*, 100632. [[CrossRef](#)]
6. Wulf, C.; Zapp, P.; Schreiber, A. Review of power-to-X demonstration projects in Europe. *Front. Energy Res.* **2020**, *8*, 191. [[CrossRef](#)]
7. Tarhan, C.; Çil, M.A. A study on hydrogen, the clean energy of the future: Hydrogen storage methods. *J. Energy Storage* **2021**, *40*, 102676. [[CrossRef](#)]
8. Capurso, T.; Stefanizzi, M.; Torresi, M.; Camporeale, S.M. Perspective of the role of hydrogen in the 21st century energy transition. *Energy Convers. Manag.* **2022**, *251*, 114898. [[CrossRef](#)]
9. Chen, G.; Feldhoff, A.; Weidenkaff, A.; Li, C.; Liu, S.; Zhu, X.; Sunarso, J.; Huang, K.; Wu, X.; Ghoniem, A.F.; et al. Roadmap for sustainable mixed ionic-electronic conducting membranes. *Adv. Funct. Mater.* **2022**, *32*, 2105702. [[CrossRef](#)]
10. Irvine, J.; Rupp, J.G.L.M.; Liu, G.; Xu, X.; Haile, S.M.; Qian, X.; Snyder, A.; Freer, R.; Ekren, D.; Skinner, S.; et al. Roadmap on inorganic perovskites for energy applications. *J. Phys. Energy* **2021**, *3*, 031502. [[CrossRef](#)]
11. Hanif, M.B.; Rauf, S.; Motola, M.; Babar, Z.U.D.; Li, C.-J.; Li, C.-X. Recent progress of perovskite-based electrolyte materials for solid oxide fuel cells and performance optimizing strategies for energy storage applications. *Mater. Res. Bull.* **2022**, *146*, 111612. [[CrossRef](#)]

12. Zhigachev, A.O.; Rodaev, V.V.; Zhigacheva, D.V.; Lyskov, N.V.; Shchukina, M.A. Doping of scandia-stabilized zirconia electrolytes for intermediate-temperature solid oxide fuel cell: A review. *Ceram. Int.* **2021**, *47*, 32490–32504. [CrossRef]
13. Saarinen, V.; Pennanen, J.; Kotisaari, M.; Thomann, O.; Himanen, O.; Di Iorio, S.; Hanoux, P.; Aicart, J.; Couturier, K.; Sun, X.; et al. Design, manufacturing, and operation of movable 2×10 kW size rSOC system. *Fuel Cells* **2021**, *21*, 477–487. [CrossRef]
14. Udomsilp, D.; Lenser, C.; Guillon, O.; Menzler, N.H. Performance benchmark of planar solid oxide cells based on material development and designs. *Energy Technol.* **2021**, *9*, 2001062. [CrossRef]
15. Zhou, Z.; Nadimpalli, V.K.; Pedersen, D.B.; Esposito, V. Degradation mechanisms of metal-supported solid oxide cells and countermeasures: A review. *Materials* **2021**, *14*, 3139. [CrossRef]
16. Khan, M.S.; Xu, X.; Knibbe, R.; Zhu, Z. Air electrodes and related degradation mechanisms in solid oxide electrolysis and reversible solid oxide cells. *Renew. Sustain. Energy Rev.* **2021**, *143*, 110918. [CrossRef]
17. Wang, Y.; Li, W.; Ma, L.; Li, W.; Liu, X. Degradation of solid oxide electrolysis cells: Phenomena, mechanisms, and emerging mitigation strategies—A review. *J. Mater. Sci. Technol.* **2020**, *55*, 35–55. [CrossRef]
18. Bello, I.T.; Zhai, S.; Zhao, S.; Li, Z.; Yu, N.; Ni, M. Scientometric review of proton-conducting solid oxide fuel cells. *Int. J. Hydrog. Energy* **2021**, *46*, 37406–37428. [CrossRef]
19. Su, H.; Hu, Y.H. Degradation issues and stabilization strategies of protonic ceramic electrolysis cells for steam electrolysis. *Energy Sci. Eng.* **2021**, 1–20. [CrossRef]
20. Shi, H.; Su, C.; Ran, R.; Cao, J.; Shao, Z. Electrolyte materials for intermediate-temperature solid oxide fuel cells. *Progr. Nat. Sci. Mater. Int.* **2020**, *30*, 764–774. [CrossRef]
21. Tarasova, N.; Animitsa, I. Materials $A^{\text{II}}\text{LnInO}_4$ with ruddlesden-popper structure for electrochemical applications: Relationship between ion (oxygen-ion, proton) conductivity, water uptake, and structural changes. *Materials* **2021**, *15*, 114. [CrossRef] [PubMed]
22. Fop, S. Solid oxide proton conductors beyond perovskites. *J. Mater. Chem. A* **2021**, *9*, 18836–18856. [CrossRef]
23. Hossain, M.K.; Biswas, M.C.; Chanda, R.K.; Rubel, M.H.K.; Khan, M.I.; Hashizume, K. A review on experimental and theoretical studies of perovskite barium zirconate proton conductors. *Emergent Mater.* **2021**, *4*, 999–1027. [CrossRef]
24. Meng, Y.; Gao, J.; Zhao, Z.; Amoroso, J.; Tong, J.; Brinkman, K.S. Review: Recent progress in low-temperature proton-conducting ceramics. *J. Mater. Sci.* **2019**, *54*, 9291–9312. [CrossRef]
25. Zamudio-García, J.; Caizán-Juanarena, L.; Porras-Vázquez, J.M.; Losilla, E.R.; Marrero-López, D. A review on recent advances and trends in symmetrical electrodes for solid oxide cells. *J. Power Sources* **2022**, *520*, 230852. [CrossRef]
26. Ni, C.; Zhou, J.; Zhang, Z.; Li, S.; Ni, J.-P.; Wu, K.; Irvine, J.T.S. Iron-based electrode materials for solid oxide fuel cells and electrolyzers. *Energy Environ. Sci.* **2021**, *14*, 6287–6319. [CrossRef]
27. Klyndyuk, A.I.; Chizhova, E.A.; Kharytonau, D.S.; Medvedev, D.A. Layered oxygen-deficient double perovskites as promising cathode materials for solid oxide fuel cells. *Materials* **2021**, *15*, 141. [CrossRef]
28. Skutina, L.; Filonova, E.; Medvedev, D.; Maignan, A. Undoped Sr_2MMoO_6 double perovskite molybdates ($M = \text{Ni}, \text{Mg}, \text{Fe}$) as promising anode materials for solid oxide fuel cells. *Materials* **2021**, *14*, 1715. [CrossRef]
29. Medvedev, D.A. Current drawbacks of proton-conducting ceramic materials: How to overcome them for real electrochemical purposes. *Curr. Opin. Green Sustain. Chem.* **2021**, *32*, 100549. [CrossRef]
30. Basu, R.N.; Tietz, F.; Wessel, E.; Buchkremer, H.P.; Stöver, D. Microstructure and electrical conductivity of $\text{LaNi}_{0.6}\text{Fe}_{0.4}\text{O}_3$ prepared by combustion synthesis routes. *Mater. Res. Bull.* **2004**, *39*, 1335–1345. [CrossRef]
31. Pikalova, E.; Bogdanovich, N.; Kolchugin, A.; Shubin, K.; Ermakova, L.; Eremeev, N.; Farlenkov, A.; Khrustov, A.; Filonova, E.; Sadykov, V. Development of composite $\text{LaNi}_{0.6}\text{Fe}_{0.4}\text{O}_{3-\delta}$ -based air electrodes for solid oxide fuel cells with a thin-film bilayer electrolyte. *Int. J. Hydrog. Energy* **2021**, *46*, 16947–16964. [CrossRef]
32. Lyagaeva, J.; Medvedev, D.; Pikalova, E.; Plaksin, S.; Brouzgou, A.; Demin, A.; Tsiakaras, P. A detailed analysis of thermal and chemical compatibility of cathode materials suitable for $\text{BaCe}_{0.8}\text{Y}_{0.2}\text{O}_{3-\delta}$ and $\text{BaZr}_{0.8}\text{Y}_{0.2}\text{O}_{3-\delta}$ proton electrolytes for solid oxide fuel cell application. *Int. J. Hydrog. Energy* **2017**, *42*, 1715–1723. [CrossRef]
33. Adachi, Y.; Hatada, N.; Kato, M.; Hirota, K.; Uda, T. Experimental validation of high electrical conductivity in Ni-rich $\text{LaNi}_{1-x}\text{Fe}_x\text{O}_3$ solid solutions ($x \leq 0.4$) in high-temperature oxidizing atmospheres. *Mater. Adv.* **2021**, *2*, 3257–3263. [CrossRef]
34. Harrison, C.M.; Slater, P.R.; Steinberger-Wilckens, R. Lanthanum nickelates and their application in solid oxide cells—The $\text{LaNi}_{1-x}\text{Fe}_x\text{O}_3$ system and other ABO_3 -type nickelates. *Solid State Ion.* **2021**, *373*, 115799. [CrossRef]
35. Hou, J.; Zhu, Z.; Qian, J.; Liu, W. A new cobalt-free proton-blocking composite cathode $\text{La}_2\text{NiO}_{4+\delta}$ - $\text{LaNi}_{0.6}\text{Fe}_{0.4}\text{O}_{3-\delta}$ for $\text{BaZr}_{0.1}\text{Ce}_{0.7}\text{Y}_{0.2}\text{O}_{3-\delta}$ -based solid oxide fuel cells. *J. Power Sources* **2014**, *264*, 67–75. [CrossRef]
36. Rietveld, H.M. A profile refinement method for nuclear and magnetic structures. *J. Appl. Crystallogr.* **1969**, *2*, 65–71. [CrossRef]
37. Roisnel, T.; Rodriguez-Carvajal, J. WinPLOTR: A windows tool for powder diffraction pattern analysis. *Mater. Sci. Forum* **2001**, *378–381*, 118–123. [CrossRef]
38. ZView® for Windows. Available online: <http://www.scribner.com/software/68-general-electrochemistr376-zview-for-windows/> (accessed on 15 February 2022).
39. An, H.; Shin, D.; Ji, H.-I. Effect of nickel addition on sintering behavior and electrical conductivity of $\text{BaCe}_{0.35}\text{Zr}_{0.5}\text{Y}_{0.15}\text{O}_{3-\delta}$. *J. Korean Ceram. Soc.* **2019**, *56*, 91–97. [CrossRef]
40. Liu, Y.; Yang, L.; Liu, M.; Tang, Z.; Liu, M. Enhanced sinterability of $\text{BaZr}_{0.1}\text{Ce}_{0.7}\text{Y}_{0.1}\text{O}_{3-\delta}$ by addition of nickel oxide. *J. Power Sources* **2011**, *196*, 9980–9984. [CrossRef]

41. Gorbova, E.; Maragou, V.; Medvedev, D.; Demin, A.; Tsiakaras, P. Influence of sintering additives of transition metals on the properties of gadolinium-doped barium cerate. *Solid State Ion.* **2008**, *179*, 887–890. [[CrossRef](#)]
42. Basbus, J.F.; Caneiro, A.; Suescun, L.; Lamas, D.G.; Moggi, L.V. Anomalous X-ray diffraction study of Pr-substituted BaCeO_{3-δ}. *Acta Crystallogr. Sect. B Struct. Sci. Cryst. Eng. Mater.* **2015**, *71*, 455–462. [[CrossRef](#)]
43. Wang, B.; Bi, L.; Zhao, X.S. Exploring the role of NiO as a sintering aid in BaZr_{0.1}Ce_{0.7}Y_{0.2}O_{3-δ} electrolyte for proton-conducting solid oxide fuel cells. *J. Power Sources* **2018**, *399*, 207–214. [[CrossRef](#)]
44. Xie, H.-H.; Gao, Q.; Li, L.; Lei, G.; Hu, X.-R.; Deng, J.-B. First-principles study of structural, electronic, magnetic and thermodynamic properties of the double perovskite Ba₂CeCoO₆. *Solid State Commun.* **2016**, *239*, 49–54. [[CrossRef](#)]
45. Moriga, T.; Hayashi, M.; Sakamoto, T.; Orihara, M.; Nakabayashi, I. Reduction processes of rare-earth nickelate perovskites LnNiO₃ (Ln=La, Pr, Nd). *Solid State Ion.* **2002**, *154–155*, 251–255. [[CrossRef](#)]
46. Kostoglouidis, G.C.; Ftikos, C. Structural, thermal and electrical properties of Pr_{0.5}Sr_{0.5}Co_{1-y}Ni_yO_{3-δ} perovskite-type oxides. *Solid State Ion.* **1998**, *109*, 43–53. [[CrossRef](#)]
47. Shannon, R.D. Revised effective ionic radii and systematic studies of interatomic distances in halides and chalcogenides. *Acta Crystallogr. Sec. A* **1976**, *32*, 751–767. [[CrossRef](#)]
48. Świerczek, K.; Marzec, J.; Pa'ubiak, D.; Zaja, W.; Molenda, J. LFN and LSCFN perovskites—Structure and transport properties. *Solid State Ion.* **2006**, *177*, 1811–1817. [[CrossRef](#)]
49. Vibhu, V.; Flura, A.; Nicollet, C.; Fourcade, S.; Penin, N.; Bassat, J.-M.; Grenier, J.-C.; Rougier, A.; Pouchard, M. Characterization of PrNiO_{3-δ} as oxygen electrode for SOFCs. *Solid State Sci.* **2018**, *81*, 26–31. [[CrossRef](#)]
50. Vashook, V.; Rebello, J.; Chen, J.Y.; Vasylechko, L.; Trots, D.; Zosel, J.; Guth, U. Thermal expansion, oxygen non-stoichiometry and diffusion mobility in some ferrites-nickelites. *Solid State Phenom.* **2013**, *200*, 86–92. [[CrossRef](#)]
51. Rebello, J.; Vashook, V.; Trots, D.; Guth, U. Thermal stability, oxygen non-stoichiometry, electrical conductivity and diffusion characteristics of PrNi_{0.4}Fe_{0.6}O_{3-δ}, a potential cathode material for IT-SOFCs. *J. Power Sources* **2011**, *196*, 3705–3712. [[CrossRef](#)]
52. Hashimoto, S.; Kammer, K.; Larsen, P.H.; Poulsen, F.W.; Mogensen, M. A study of Pr_{0.7}Sr_{0.3}Fe_{1-x}Ni_xO_{3-δ} as a cathode material for SOFCs with intermediate operating temperature. *Solid State Ion.* **2005**, *176*, 1013–1020. [[CrossRef](#)]
53. Tsipis, E.; Kiselev, E.; Kolotygin, V.; Waerenborgh, J.; Cherepanov, V.; Kharton, V. Mixed conductivity, Mössbauer spectra and thermal expansion of (La,Sr)(Fe,Ni)O_{3-δ} perovskites. *Solid State Ion.* **2008**, *179*, 2170–2180. [[CrossRef](#)]
54. Sakaki, Y. Ln_{1-x}Sr_xMnO₃ (Ln=Pr, Nd, Sm and Gd) as the cathode material for solid oxide fuel cells. *Solid State Ion.* **1999**, *118*, 187–194. [[CrossRef](#)]
55. Lyagaeva, Y.G.; Medvedev, D.A.; Demin, A.V.K.; Tsiakaras, P.; Reznitskikh, O.G. Thermal expansion of materials in the barium cerate-zirconate system. *Phys. Solid State* **2015**, *57*, 285–289. [[CrossRef](#)]
56. Flura, A.; Dru, S.; Nicollet, C.; Vibhu, V.; Fourcade, S.; Lebraud, E.; Rougier, A.; Bassat, J.-M.; Grenier, J.-C. Chemical and structural changes in Ln₂NiO_{4+δ} (Ln=La, Pr or Nd) lanthanide nickelates as a function of oxygen partial pressure at high temperature. *J. Solid State Chem.* **2015**, *228*, 189–198. [[CrossRef](#)]
57. Chiba, R.; Yoshimura, F.; Sakurai, Y. An investigation of LaNi_{1-x}Fe_xO₃ as a cathode material for solid oxide fuel cells. *Solid State Ion.* **1999**, *124*, 281–288. [[CrossRef](#)]
58. Gateshki, M.; Suescun, L.; Kolesnik, S.; Mais, J.; Świerczek, K.; Short, S.; Dabrowski, B. Structural, magnetic and electronic properties of LaNi_{0.5}Fe_{0.5}O₃ in the temperature range 5–1000K. *J. Solid State Chem.* **2008**, *181*, 1833–1839. [[CrossRef](#)]
59. Niwa, E.; Uematsu, C.; Miyashita, E.; Ohzeki, T.; Hashimoto, T. Conductivity and sintering property of LaNi_{1-x}Fe_xO₃ ceramics prepared by Pechini method. *Solid State Ion.* **2011**, *201*, 87–93. [[CrossRef](#)]
60. Hashimoto, S.; Kammer, K.; Poulsen, F.W.; Mogensen, M. Conductivity and electrochemical characterization of PrFe_{1-x}Ni_xO_{3-δ} at high temperature. *J. Alloy. Compd.* **2007**, *428*, 256–261. [[CrossRef](#)]
61. Wu, M.; Cai, H.; Jin, F.; Sun, N.; Xu, J.; Zhang, L.; Han, X.; Wang, S.; Su, X.; Long, W.; et al. Assessment of cobalt-free ferrite-based perovskite Ln_{0.5}Sr_{0.5}Fe_{0.9}Mo_{0.1}O_{3-δ} (Ln = lanthanide) as cathodes for IT-SOFCs. *J. Eur. Ceram. Soc.* **2021**, *41*, 2681–2690. [[CrossRef](#)]
62. Tarutin, A.P.; Vdovin, G.K.V.; Medvedev, D.A.; Yaremchenko, A.A. Fluorine-containing oxygen electrodes of the nickelate family for proton-conducting electrochemical cells. *Electrochim. Acta* **2020**, *337*, 135808. [[CrossRef](#)]
63. Nasani, N.; Ramasamy, D.; Antunes, I.; Singh, B.; Fagg, D.P. Structural and electrical properties of strontium substituted Y₂BaNiO₅. *J. Alloy. Compd.* **2015**, *620*, 91–96. [[CrossRef](#)]
64. Tarutin, A.P.; Lyagaeva, Y.G.; Vylkov, A.I.; Gorshkov, M.Y.; Vdovin, G.K.V.; Medvedev, D.A. Performance of Pr₂(Ni,Cu)O_{4+δ} electrodes in protonic ceramic electrochemical cells with unseparated and separated gas spaces. *J. Mater. Sci. Technol.* **2021**, *93*, 157–168. [[CrossRef](#)]
65. Huang, S.; Lu, Q.; Feng, S.; Li, G.; Wang, C. PrNi_{0.6}Co_{0.4}O₃-Ce_{0.8}Sm_{0.2}O_{1.9} composite cathodes for intermediate temperature solid oxide fuel cells. *J. Power Sources* **2012**, *199*, 150–154. [[CrossRef](#)]
66. Li, Y.; Cai, J.W.; Alonso, J.A.; Lian, H.Q.; Cui, X.G.; Goodenough, J.B. Evaluation of LaNi_{0.6}M_{0.4}O₃ (M = Fe, Co) cathodes in LSGM-electrolyte-supported solid-oxide fuel cells. *Int. J. Hydrog. Energy* **2017**, *42*, 27334–27342. [[CrossRef](#)]
67. Bevilacqua, M.; Montini, T.; Tavagnacco, C.; Fonda, E.; Fornasiero, P.; Graziani, M. Preparation, characterization, and electrochemical properties of pure and composite LaNi_{0.6}Fe_{0.4}O₃-based cathodes for IT-SOFC. *Chem. Mater.* **2007**, *19*, 5926–5936. [[CrossRef](#)]
68. Chrzan, A.; Karczewski, J.; Gazda, M.; Szymczewska, D.; Jasinski, P. Investigation of thin perovskite layers between cathode and doped ceria used as buffer layer in solid oxide fuel cells. *J. Solid State Electrochem.* **2015**, *19*, 1807–1815. [[CrossRef](#)]

69. Khoshkalam, M.; Faghihi-Sani, M.A.; Tong, X.; Chen, M.; Hendriksen, P.V. Enhanced Activity of Pr_6O_{11} and CuO Infiltrated $\text{Ce}_{0.9}\text{Gd}_{0.1}\text{O}_2$ Based Composite Oxygen Electrodes. *J. Electrochem. Soc.* **2020**, *167*, 024505. [[CrossRef](#)]
70. Chrzan, A.; Ovtar, S.; Chen, M. $\text{LaNi}_{1-x}\text{Co}_x\text{O}_{3-\delta}$ ($x = 0.4$ to 0.7) cathodes for solid oxide fuel cells by infiltration. *IOP Conf. Ser. Mater. Sci. Eng.* **2016**, *104*, 012019. [[CrossRef](#)]
71. Hjalmarsson, P.; Mogensen, M. $\text{La}_{0.99}\text{Co}_{0.4}\text{Ni}_{0.6}\text{O}_{3-\delta}-\text{Ce}_{0.8}\text{Gd}_{0.2}\text{O}_{1.95}$ as composite cathode for solid oxide fuel cells. *J. Power Sources* **2011**, *196*, 7237–7244. [[CrossRef](#)]
72. Huang, S.; Feng, S.; Wang, H.; Li, Y.; Wang, C. $\text{LaNi}_{0.6}\text{Fe}_{0.4}\text{O}_3-\text{Ce}_{0.8}\text{Sm}_{0.2}\text{O}_{1.9}-\text{Ag}$ composite cathode for intermediate temperature solid oxide fuel cells. *Int. J. Hydrog. Energy* **2011**, *36*, 10968–10974. [[CrossRef](#)]
73. Natalia Popova's Web-Sites. Scientific Translation Laboratory. Available online: <https://nauka-perevod.ru> (accessed on 15 February 2022).